nature communications

Article

https://doi.org/10.1038/s41467-026-68835-0

Fatigue resistant elastocaloric effect in TiNi via texture-precipitate synergy

Received: 18 April 2025

Accepted: 13 January 2026

Published online: 29 January 2026

Check for updates

Xu Li[1,2], Qianglong Liang[1,2] ✉, Chuanxin Liang[1], Dong Wang[1], Suzhi Li[1] & Xiangdong Ding[1] ✉

Shape memory alloys with both a large elastocaloric effect and exceptional fatigue resistance are key candidates for next-generation solid-state cooling technologies. Here, we report a textured TiNi alloy containing engineered Ti_4Ni_2O precipitates, fabricated via controlled directional solidification, that achieves a large adiabatic temperature change of −15.9 K after 10 million compressive cycles. Microstructural analyses reveal columnar B2 grains aligned with the solidification direction and a uniform dispersion of high-density Ti_4Ni_2O precipitates. A strong crystallographic texture is observed, enabling a large transformation strain of over 6% under compressive loading, as mapped by digital image correlation. In-situ loading X-ray diffraction confirms a continuous increase in intensity of B19′ martensite under stress, while in-situ cooling transmission electron microscopy captures numerous nucleation and progressive growth of the B19′ martensite from B2/Ti_4Ni_2O interfaces. High-resolution TEM further reveals localized lattice distortions at these interfaces, promoting directional and confined growth of B19′ martensite. This progressive transformation, which preserves functional reversibility, combined with the mutual texture–precipitate architecture that enhances mechanical stability, gives rise to ultrahigh fatigue life. These findings highlight the promise of textured TiNi with tailored precipitate architecture for long-term elastocaloric applications and provide a design strategy for developing fatigue-resistant SMAs through microstructural and textural engineering.

Refrigeration is a cornerstone of modern infrastructure, enabling technologies from food preservation to electronics and medical systems[1]. However, conventional vapor compression systems are nearing their theoretical efficiency limits and rely on refrigerants with high global warming potential, raising serious environmental concerns[2,3]. These challenges have spurred the development of sustainable, high-efficiency solid-state cooling technologies. Among these, elastocaloric cooling, which leverages the reversible martensitic transformation in shape memory alloys (SMAs), has emerged as a particularly promising solution due to its high energy efficiency and environmentally benign nature[4–8].

The elastocaloric effect is driven by the latent heat exchange associated with stress-induced martensitic transformation[9], with performance typically quantified by the adiabatic temperature change (ΔT_{ad}) [10,11]. TiNi-based SMAs are among the most extensively studied due to their excellent mechanical and functional properties[12,13]. However, real-world elastocaloric applications require these materials to maintain functionality over millions of mechanical cycles[14]. TiNi alloys, in particular, are susceptible to both structural fatigue—leading to fracture—and functional fatigue, characterized by a decline in elastocaloric performance over time[15,16]. Thus, achieving both a large elastocaloric response and long-term cyclic durability remains a fundamental challenge.

[1]State Key Laboratory for Mechanical Behavior of Materials, Xi'an Jiaotong University, Xi'an, Shaanxi, China. [2]These authors contributed equally: Xu Li, Qianglong Liang. ✉e-mail: liangqianglong@xjtu.edu.cn; dingxd@xjtu.edu.cn

A variety of strategies have been explored to address this issue, including compositional tuning, grain refinement, precipitation hardening, and composite architectures[17–24]. Among these, precipitation engineering has shown particular promise[21,22,25]. Strengthening phases such as Ti_2Cu[17], Ti_2Ni[26,27], Ti_2Ni_3[22], and $TiNi_3$[21] have been introduced to enhance fatigue life by promoting transformation reversibility at matrix–precipitate interfaces. However, excessive precipitation can hinder martensitic transformation, thereby diminishing the elastocaloric response[21,22]. Thus, optimizing the balance between mechanical strengthening and transformation compatibility is essential.

Crystallographic orientation also plays a critical role in dictating the functional response of TiNi alloys. Shape memory and superelastic behaviors are both strongly orientation-dependent[28,29], and this extends to elastocaloric performance. Techniques such as cold rolling and directional solidification have been used to induce strong texture, with significant variation in elastocaloric response observed along different loading directions[30–32]. Recent reports of high elastocaloric performance in highly textured Heusler alloys and Ti-based SMAs—including NiMnTi and Ti-Nb-Zr-Ta—as well as enhanced stability in tweed-textured Fe-Pd single crystals, highlight the power of texture control[33–40]. Yet, limited attention has been paid to integrating crystallographic texture with microstructural engineering to improve fatigue resistance in elastocaloric TiNi alloys.

Notably, TiNi alloys exhibit strong mechanical asymmetry: while $<001>_{B2}$-oriented grains show limited transformation under tension, they exhibit large recoverable strains under compression[41,42]. Moreover, introducing coherent precipitates with specific orientation relationships has been shown to promote reversible martensitic transformation and suppress fatigue damage by enabling martensite nucleation via localized lattice distortions[17,21,22]. These insights suggest that co-designing texture and precipitate architecture could be a powerful strategy to simultaneously achieve high elastocaloric performance and exceptional fatigue resistance.

Here, we report a textured $Ti_{49}Ni_{51}$ (at. %) alloy with high-density, epitaxially aligned Ti_4Ni_2O precipitates, synthesized via controlled directional solidification. The alloy exhibits a large ΔT_{ad} of −15.9 K, sustained over 10^7 compressive loading-unloading cycles. This performance is proposed to derive from synergistic effects of strong crystallographic texture and a distributed martensitic transformation enabled by interfacial lattice distortions at B2/Ti_4Ni_2O boundaries. These findings underscore the promise of texture–precipitate co-design in TiNi-based SMAs and offer a viable pathway for developing durable, high-performance elastocaloric materials for solid-state cooling.

Results

Textured microstructure with aligned Ti_4Ni_2O precipitates enables large and stable transformation strain

The microstructure of the directionally solidified $Ti_{49}Ni_{51}$ alloy was first characterized using scanning electron microscopy (SEM). Backscattered electron (BSE) images captured along and perpendicular to the solidification direction (SD) reveal a highly textured structure comprising columnar grains oriented along the SD (Fig. 1a, b). The grain lengths exceed millimeter with widths ranging from tens to hundreds of micrometers. Strong contrast variation between grains in the cross-sectional view (perpendicular to SD) indicates substantial orientation differences, whereas the longitudinal section (parallel to SD) exhibits minimal contrast, suggesting a preferred grain orientation along the SD. Notably, fine precipitates are uniformly distributed throughout the columnar grains, aligned along the SD, and without significant segregation near grain boundaries.

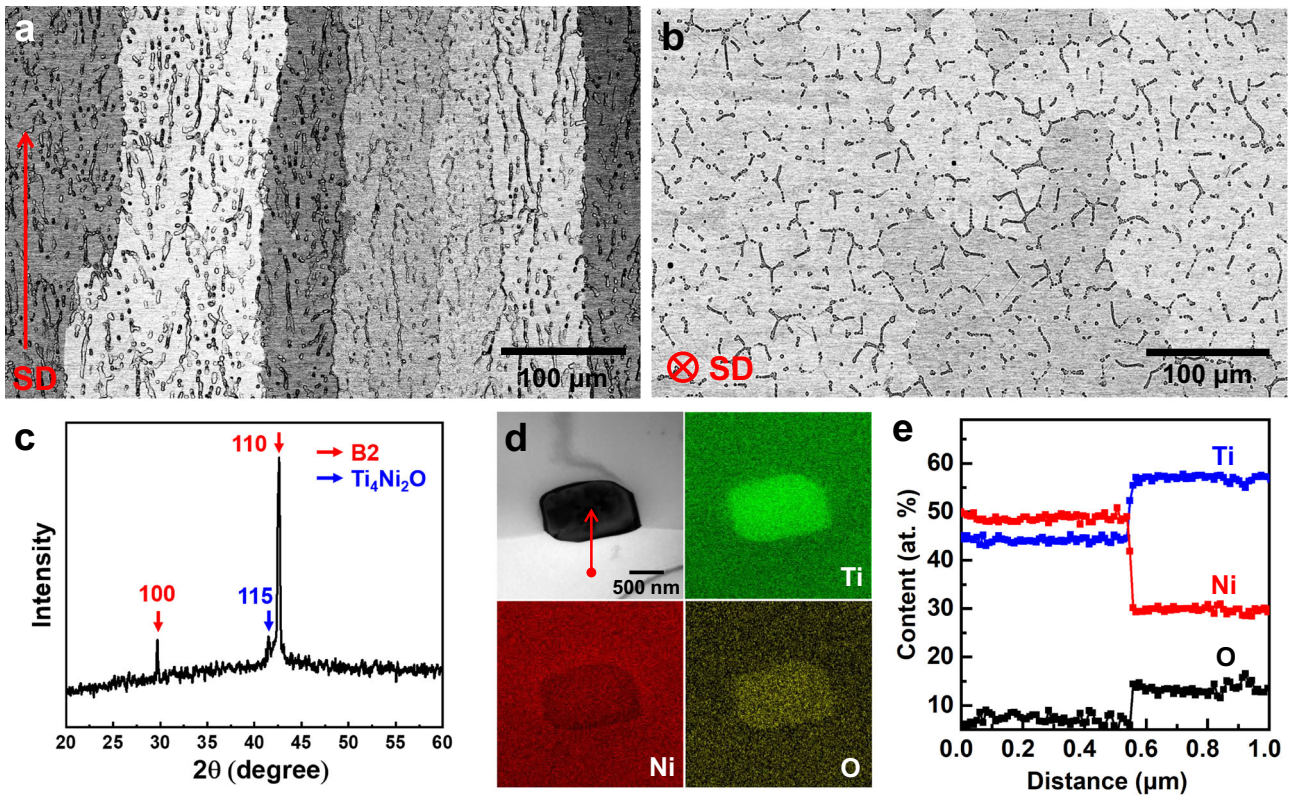

Fig. 1 | Microstructural characterization of the as-prepared $Ti_{49}Ni_{51}$ alloy. BSE SEM images acquired parallel (**a**) and perpendicular (**b**) to the SD, revealing a columnar grain structure aligned with SD. **c** XRD pattern confirms the coexistence of the B2 matrix and Ti_4Ni_2O precipitates. **d** Bright-field TEM image with corresponding EDS elemental maps, highlighting the composition of the Ti_4Ni_2O precipitate embedded within the B2 matrix. **e** EDS line scan along the red arrow in (**d**), showing the elemental distribution and interface sharpness across the matrix–precipitate boundary. Source data are provided as a Source Data file.

https://doi.org/10.1038/s41467-026-68835-0

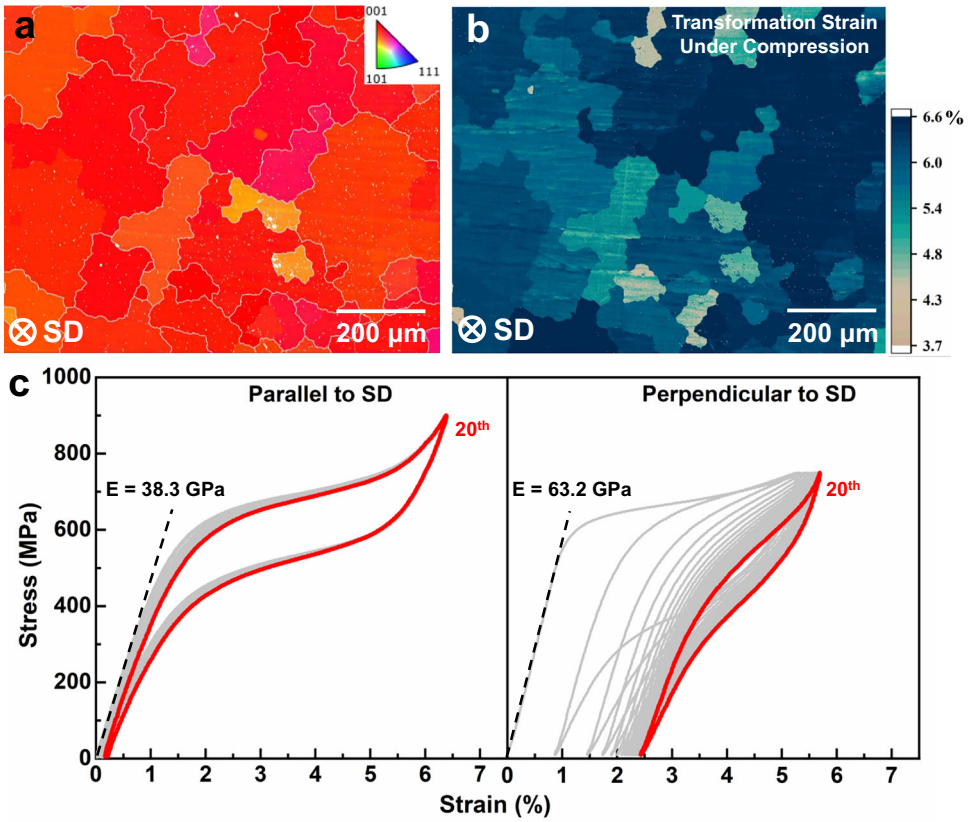

Fig. 2 | Textured microstructure and orientation-dependent mechanical behavior. a IPF orientation map of the B2 phase acquired on a cross-section perpendicular to the SD, revealing a strong texture along the SD. The corresponding IPF color legend is shown in the inset. **b** Theoretical transformation strain map under compression along SD, derived from the orientation data in (**a**) based on the crystallographic relationship between the B2 parent phase and B19′ martensite. The average calculated transformation strain reaches 6.1%. **c** Ambient temperature compressive stress–strain curves measured parallel and perpendicular to SD, highlighting significant anisotropy in mechanical response and enhanced superelasticity along SD. Source data are provided as a Source Data file.

X-ray diffraction (XRD) confirms the presence of the B2 austenite phase along with a secondary phase indexed as Ti_4Ni_2O (Fig. 1c). No martensitic phase is detected at room temperature. The Ti_4Ni_2O phase adopts a cubic structure (space group $Fd\bar{3}m$), similar to the Ti_2Ni phase, with only slight differences in lattice parameters[43,44]. To further identify the chemical composition of the precipitates, scanning/transmission electron microscopy (S/TEM) coupled with energy-dispersive X-ray spectroscopy (EDS) was performed. A representative bright-field TEM image (Fig. 1d) shows a submicron precipitate embedded in the matrix. Elemental mapping and line profile analysis across the interface (Fig. 1e) reveal that the precipitate is enriched in Ti and O but depleted in Ni, with an approximate atomic ratio of Ti:Ni:O = 4:2:1. This confirms the formation of Ti_4Ni_2O precipitates coherently embedded within the B2 matrix.

Electron backscatter diffraction (EBSD) analysis performed on the transverse cross-section (perpendicular to SD) reveals a strong crystallographic texture in both the B2 matrix and the Ti_4Ni_2O precipitates. The inverse pole figure (IPF) map (Fig. 2a) indicates a predominant orientation close to $<001>_{B2}$ aligned with the SD. Several discrete submicron regions are identified as Ti_4Ni_2O precipitates (Supplementary Fig. S1), which also share the <001> orientation. Pole figure (PF) analysis confirms an identical orientation relationship between the matrix and precipitates: $\{001\}<110>_{B2}$ // $\{001\}<110>_{Ti_4Ni_2O}$ (Figure S2). This mutual texture supports the epitaxial growth of Ti_4Ni_2O precipitates within the preferentially oriented B2 grains during directional solidification.

Given the orientation-dependent transformation behavior in TiNi alloys, the local transformation strain was analyzed based on the measured orientation distribution and the known crystallography of the B2 to B19′ martensitic transformation[12]. A two-dimensional transformation strain map derived from the grain orientation data (Fig. 2b, Supplementary Fig. S3) shows an average theoretical transformation strain of ~6.1% under compression along the SD, with minor variations across different grains due to slight orientation deviations. Theoretical averaged transformation strains for arbitrary loading directions were computed from EBSD data and indicate a clear orientation preference (Figure S3).

To assess the mechanical response, superelastic cycling tests were conducted at room temperature in both parallel and perpendicular directions relative to the SD. Samples tested along the SD exhibit a large recoverable strain of up to 6.2%, maintaining stable superelasticity over repeated cycles (Fig. 2c). In contrast, samples tested perpendicular to the SD accumulate significant residual strain within 20 cycles (Fig. 2c), indicating poor functional stability. Comparing experimental results with these theoretical averages in Fig. S3, the measured compressive strain along the SD (6.2%) corresponds to ~102% of the theoretical average (6.1%), with the slight excess (~0.1%) attributable to elastic strain under high applied stress. In contrast, the strain perpendicular to the SD decreases from 4.5% initially to a stabilized value of 3.2% after 20 cycles, corresponding to ~80% and ~57% of the theoretical average (5.6%), respectively. The parallel direction also shows a nonlinear, narrow hysteresis superelastic response without a pronounced stress plateau, accompanied by a reduced elastic modulus (~38.3 GPa) compared to the perpendicular direction (~63.2 GPa). This reduced modulus and diminished hysteresis suggest a regulated and anisotropic martensitic transformation under the texture-precipitate synergy. These results highlight the superior cyclic stability and recoverability of the textured direction, which is critical for long-term elastocaloric performance.

https://doi.org/10.1038/s41467-026-68835-0

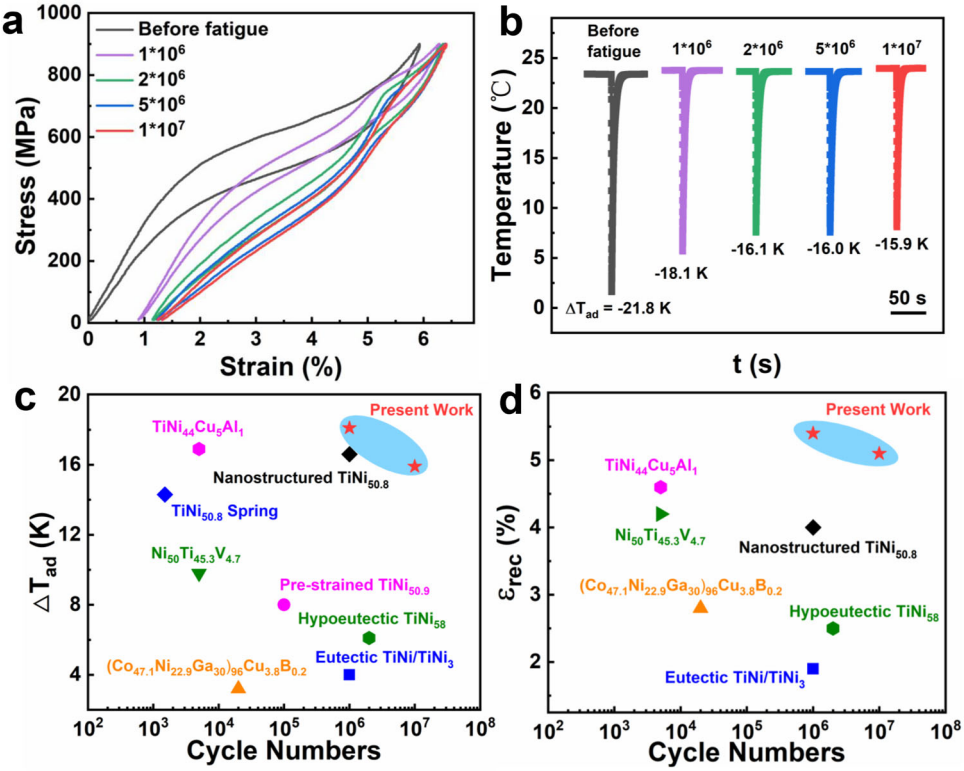

Fig. 3 | Fatigue endurance and elastocaloric performance of the textured $Ti_{49}Ni_{51}$ alloy under compression along the SD. a Superelastic stress–strain curves obtained after various numbers of compressive fatigue cycles at a maximum stress of 900 MPa, demonstrating excellent strain recoverability. **b** Evolution of the ΔT_{ad} after the same number of cycles as in (**a**), recorded under rapid unloading from 900 MPa, indicating stable elastocaloric response. **c**, **d** Comparison of the fatigue performance of ΔT_{ad} and recoverable strain (ε_{rec}) in the textured $Ti_{49}Ni_{51}$ alloy with reported bulk SMAs, including nanostructured $TiNi_{50.8}$ alloy[19], TiNi/$TiNi_3$ eutectic TiNi alloy[21], hypoeutectic $TiNi_{58}$ alloy[22], nanocrystalline Ti-44Ni-5Cu-1Al alloy[23], $TiNi_{50.8}$ spring[45], polycrystalline $Ni_{50}Ti_{45.3}V_{4.7}$ alloy[46], pre-strained $TiNi_{50.9}$ plates[47], Cu and B co-doped Co-Ni-Ga alloy[48], highlighting the superior fatigue resistance and elastocaloric stability of the present work. Source data are provided as a Source Data file.

Elastocaloric effect with high fatigue life

The elastocaloric performance and fatigue resistance of the textured $Ti_{49}Ni_{51}$ alloy were evaluated via cyclic compressive loading along the textured direction (parallel to the SD) at room temperature. As shown in Fig. 3a, b, the alloy exhibits exceptional durability, enduring up to 10^7 compressive cycles without fracture. Despite minor attenuation of the superelastic response over cycling, the stress–strain curves (Fig. 3a) show a substantial recoverable strain of 5.1% after 10^7 cycles, with total residual strain of ~0.75%. Both the hysteresis and elastic modulus decrease gradually during cycling, suggesting evolving but stable transformation behavior. A crossover emerges at ~4% strain in the stress–strain curves after ~10^6 cycles, originating from the onset of a two-step transformation (Figure S11). The ΔT_{ad}, a direct measure of the elastocaloric effect, was also monitored throughout the fatigue life (Fig. 3b). Initially, the alloy delivers a large ΔT_{ad} of −21.8 K. After an initial drop of 5.7 K within the first 2 × 10^6 cycles, ΔT_{ad} stabilizes, decreasing by only 0.2 K over the remaining 8 × 10^6 cycles. This stabilization indicates that most performance degradation occurs early in cycling, after which the elastocaloric response remains largely constant, highlighting excellent long-term functional reliability.

A comparative analysis of bulk SMAs reported in literature[19,21–23,45–48] (Fig. 3c) underscores the exceptional balance achieved in this textured $Ti_{49}Ni_{51}$ alloy. Unlike typical SMAs that display a trade-off between elastocaloric strength and fatigue life, the present material simultaneously exhibits an ultrahigh fatigue life (10^7 cycles), a substantial elastocaloric effect (ΔT_{ad} = −15.9 K), and a large coefficient of material (COP_{mat} = 23.7 after fatigue, Figure S5). Moreover, a relatively low compressive driving stress of ≈900 MPa is sufficient to induce complete transformation in our textured $Ti_{49}Ni_{51}$ alloy compared with several strengthened TiNi systems[19,21,22], reducing mechanical energy input and enhancing potential for practical applications, although further optimization is required for commercialization. Importantly, the recoverable strain remains significant even after extended cycling (Fig. 3d), further supporting the material's robust functional endurance. These combined attributes—large and stable ΔT_{ad}, long fatigue life, high COP_{mat}—establish the textured $Ti_{49}Ni_{51}$ alloy as a highly promising candidate for durable elastocaloric cooling applications.

Uniform and progressive martensitic transformation upon loading

To elucidate the origin of the ultrahigh fatigue resistance, the phase transformation behavior during loading was characterized in detail. Digital image correlation (DIC) mapping of strain fields (Fig. 4a) reveals a transformation strain distribution of over 6% under compression. While local strain variations are present, the overall transformation field is more spatially uniform compared with the pronounced strain localization and Lüders-like banding during stress-induced martensitic transformation (SIMT) typically observed in conventional TiNi alloys[49,50]. This observation aligns with the previously reported nonlinear stress–strain response lacking a distinct plateau (Fig. 2), consistent with macroscopically uniform transformation phenomena observed in select TiNi alloys[51,52].

To further probe the transformation pathway, in-situ XRD analysis was performed under incremental compressive stress up to 900 MPa (Fig. 4b). Initially, diffraction peaks correspond exclusively to the B2 parent phase and Ti_4Ni_2O precipitates. As stress increases, peaks associated with B19′ martensite gradually appear and intensify, while

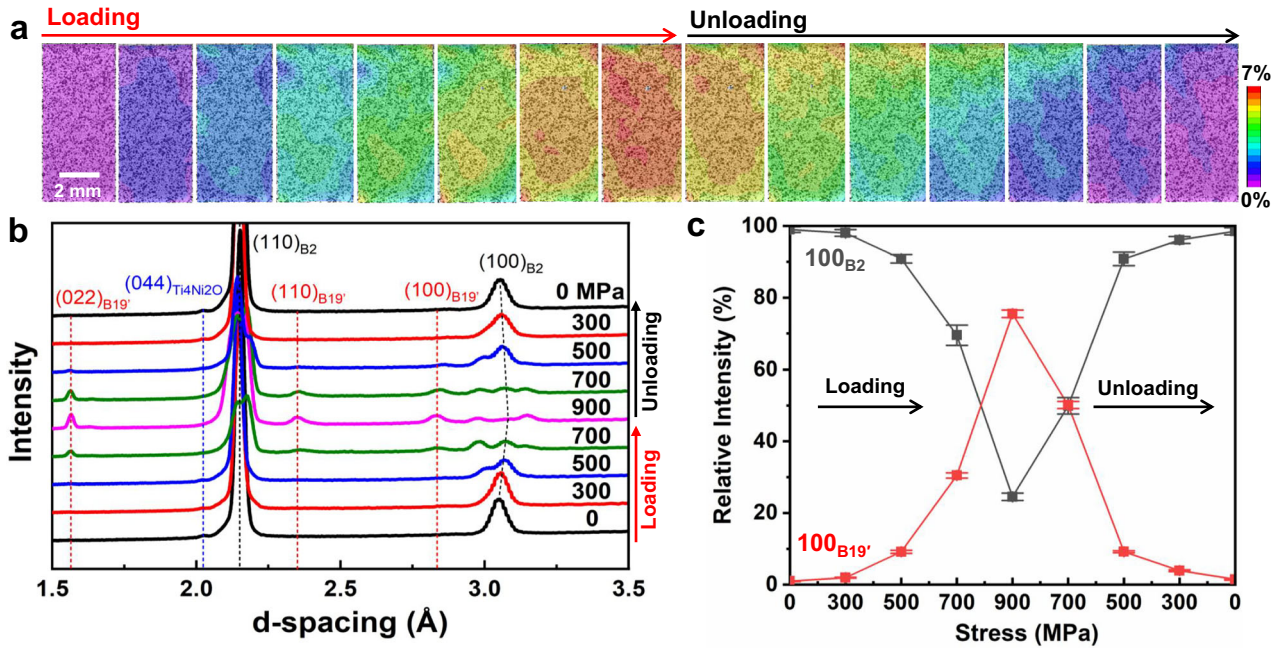

Fig. 4 | Uniform and progressive martensitic transformation under compressive loading in the textured $Ti_{49}Ni_{51}$ alloy. a DIC strain maps captured during compressive loading and unloading up to 900 MPa reveal spatially uniform transformation strain distribution, indicating a homogeneous transformation process. **b** In-situ XRD patterns acquired under stepwise compressive loading and unloading show a gradual evolution of diffraction peaks corresponding to the B2 and B19′ phases. **c** Relative diffraction intensities of the $(100)_{B2}$ and $(100)_{B19'}$ reflections are extracted from peak area analyses, illustrating a smooth and progressive transformation between B2 and B19′ phases during the loading-unloading cycle. The relative diffraction intensity of $(100)_{B2}$ and $(100)_{B19'}$ are defined as $\frac{I(100)_{B2}}{I(100)_{B2}+I(100)_{B19'}} \times 100\%$ and $\frac{I(100)_{B19'}}{I(100)_{B2}+I(100)_{B19'}} \times 100\%$, respectively. The error bars represent the standard error obtained from peak analysis. Source data are provided as a Source Data file.

those of the B2 phase diminish. Upon unloading, the diffraction profile nearly returns to its original state, confirming a highly reversible martensitic transformation with minimal retained martensite. The evolution of the $(100)_{B2}$ and $(100)_{B19'}$ peak intensities is plotted in Fig. 4c. The relative intensity of $(100)_{B19'}$ increases smoothly with stress beyond 500 MPa, reaching a maximum at peak load, and then gradually diminishes during unloading. This gradual and continuous evolution confirms the absence of abrupt martensite nucleation or burst-like propagation, distinguishing the transformation from classical SIMT and indicating a diffuse, progressive transformation mechanism. To avoid confusion with the strict thermodynamic concept of a second-order transition, we use 'progressive' or 'distributed' transformation to denote a macroscopically smooth, multi-site B2 → B19′ transformation that proceeds over a wide stress interval while retaining two-phase coexistence at microscopic length scales. Such a progressive phase transformation under wide stress range minimizes internal stress concentrations and reduces microstructural damage, thereby enhancing transformation reversibility and fatigue life. The progressive martensite formation and reversion also help suppress defect accumulation that typically degrades performance in conventional SMAs. These insights underscore the pivotal role of microstructure-controlled transformation pathways in achieving superior fatigue resistance, warranting further investigation into the nanoscale characteristics governing this behavior.

Promoted nucleation and confined growth of martensite under lattice distortions near B2/Ti_4Ni_2O interface

To clarify the underlying microstructural mechanism responsible for the observed transformation behavior, in-situ TEM observations were performed during cooling from 315 K to 105 K. As shown in Fig. 5a, the microstructure at 315 K—well above the martensitic transformation temperature—consists of a B2 matrix with Ti_4Ni_2O precipitates. The selected-area electron diffraction (SAED) pattern (Fig. 5a′) from the red-circled region confirms the presence of a single-phase B2 matrix between precipitates at this temperature. Upon cooling to 215 K, just below the martensitic transformation start temperature, nucleation of B19′ martensite is observed in proximity to B2/Ti_4Ni_2O interfaces (Fig. 5b). The corresponding SAED pattern (Fig. 5b′) reveals the coexistence of both B2 and B19′ phases in this region, suggesting that the interface serves as a favorable nucleation site. At 105 K—below the martensitic finish temperature—the matrix between precipitates is nearly fully transformed into martensite (Fig. 5c). The SAED pattern (Fig. 5c′) confirms the presence of a single-variant B19′ martensitic structure, devoid of twinning. These observations suggest that the B2/Ti_4Ni_2O interfaces facilitate the directional nucleation and confined growth of martensite, enabling a smooth and spatially uniform transformation throughout the microstructure. The absence of twinned martensite further supports the hypothesis of interface-mediated variant selection, likely governed by strain fields at the phase boundaries.

To investigate the structural features governing this behavior, high-resolution transmission electron microscopy (HR-TEM) was employed to examine the B2/Ti_4Ni_2O interface (Fig. 6). The bright-field image (Fig. 6a) and corresponding SAED pattern (Fig. 6a′) confirm a well-defined orientation relationship of $\{100\}<011>_{B2}$ // $\{400\}<011>_{Ti_4Ni_2O}$ between the matrix and precipitate. A closer examination of the B2/Ti_4Ni_2O interface region (red square in Fig. 6a) is shown in Fig. 6b, accompanied by its Fast Fourier Transform (FFT, Fig. 6c), where the presence of streaking indicates substantial lattice distortion near the interface. Further analysis via inverse FFT (IFFT), generated by selecting the overlapping $(100)_{B2}$ and $(400)_{Ti_4Ni_2O}$ reflections (red circle in Fig. 6c) is shown in Fig. 6d, revealing a high density of dislocations localized at the interface. The lattice strain distribution near the B2/Ti_4Ni_2O boundary was quantitatively mapped using geometric phase analysis (GPA)[53], shown in Fig. 6e–g. Strain mapping reveals localized lattice distortions exceeding ±10% adjacent

https://doi.org/10.1038/s41467-026-68835-0

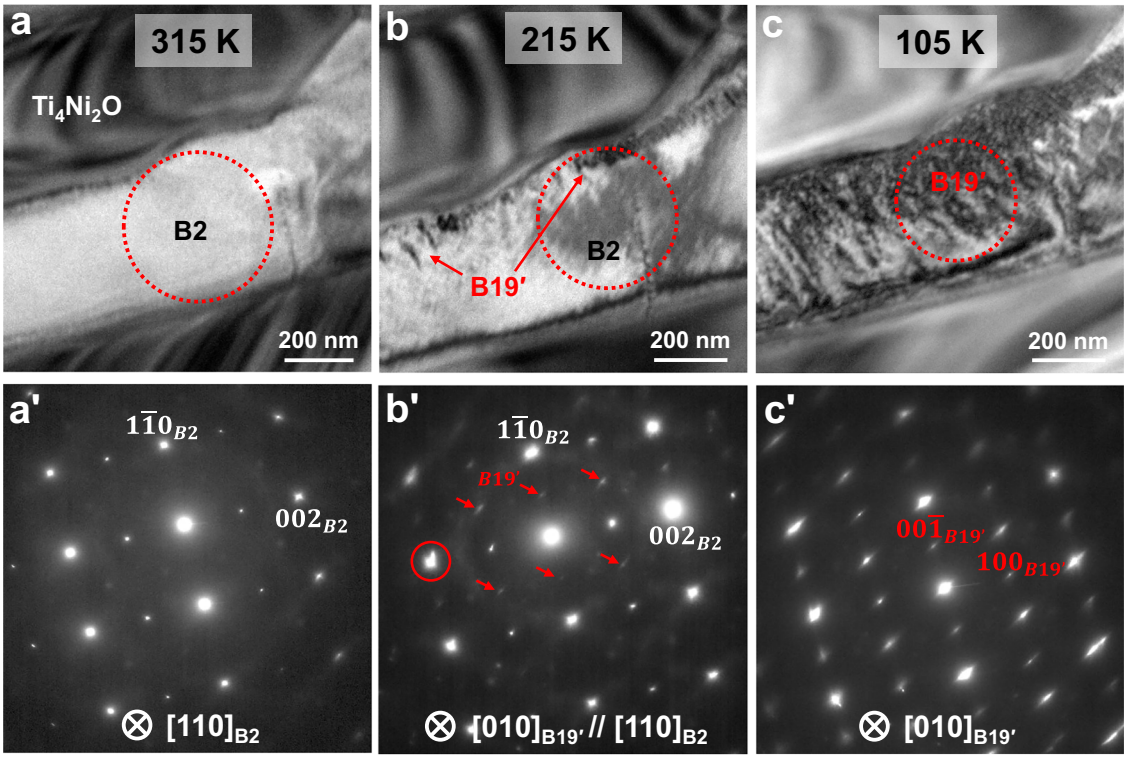

Fig. 5 | In-situ TEM observation of B19′ martensite nucleation and growth near the B2/Ti_4Ni_2O interface during cooling. Bright-field TEM images acquired at progressively decreasing temperatures of 315 K (**a**), 215 K (**b**), and 105 K (**c**) show the evolution of martensitic transformation. A nano-scale thin layer of B19′ martensite begins to nucleate near the B2/Ti_4Ni_2O interface at 215 K (**b**), with further growth observed at 105 K (**c**). **a′**–**c′** Corresponding SAED patterns taken from the region marked by red circles in (**a**–**c**). Additional diffraction spots associated with the emergent B19′ martensite phase appear in (**b′**) and are highlighted by red arrows, confirming the phase transformation onset.

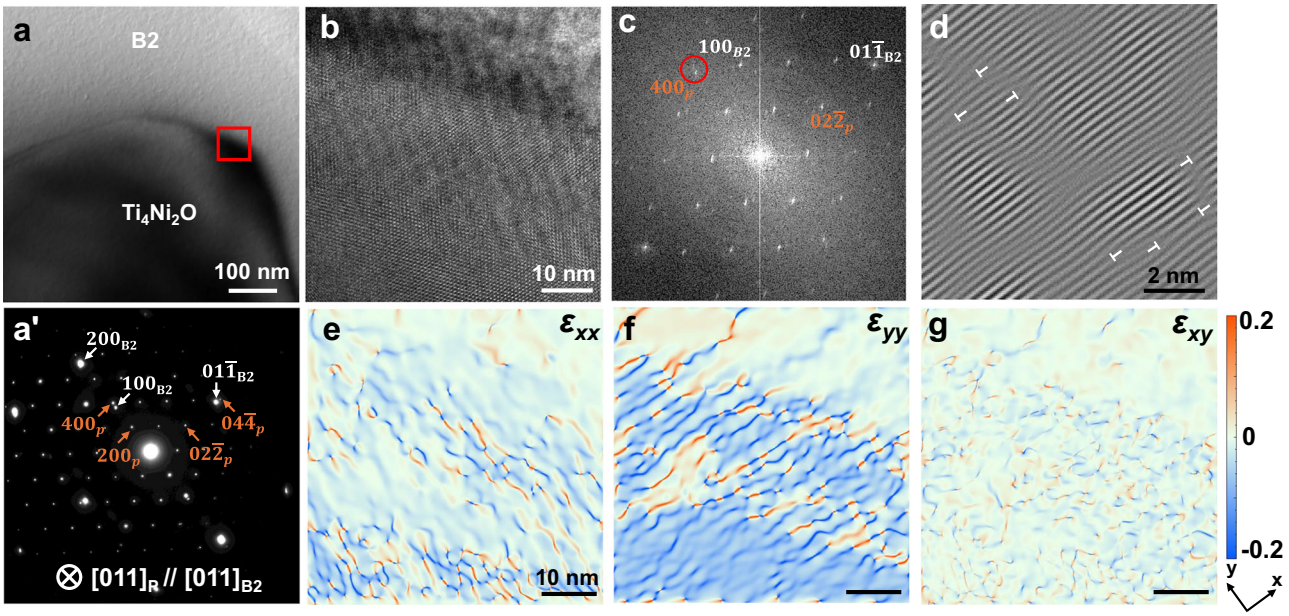

Fig. 6 | Lattice distortion near the B2/Ti_4Ni_2O interface revealed by HR-TEM. **a** Bright-field TEM image showing the boundary region between the B2 matrix and Ti_4Ni_2O precipitates. **a′** SAED pattern taken across the B2/Ti_4Ni_2O interface along the $[011]_{Ti_4Ni_2O}$ // $[011]_{B2}$ zone axis, confirming the epitaxial orientation relationship. **b** HR-TEM images focusing on the B2/Ti_4Ni_2O interface. **c** FFT reflections corresponding to **b**. **d** IFFT image generated by selecting the overlapping $(100)_{B2}$ and $(400)_{Ti_4Ni_2O}$ reflections from the FFT in (**b**), clearly revealing the presence of interfacial dislocations. **e**–**g** Two-dimensional lattice strain fields near the interface are visualized using GPA based on the HR-TEM image in (**b**) including normal strain in the x-direction (ε_{xx}), y-direction (ε_{yy}), and shear strain (ε_{xy}), respectively, demonstrating significant local lattice distortion induced by the interface. The foot note "p" in **a′** and **c** indicates signal from Ti_4Ni_2O precipitates.

to the interface, confirming the presence of intense strain fields. These distortions arise due to the lattice mismatch and dislocation accumulation at the interface, effectively lowering the energy barrier for martensite nucleation[54]. As such, these regions serve as ideal nucleation sites and provide a guiding framework for the formation and confined propagation of specific martensitic variants during cooling or mechanical loading. The combination of coherent crystallographic alignment and strain-concentrated interfacial zones enables a progressive, directional, and spatially uniform transformation process. This mechanism suppresses transformation-induced defects and enhances reversibility, ultimately contributing to the high fatigue resistance observed in the textured $Ti_{49}Ni_{51}$ alloy. The results highlight the critical role of microstructural design—particularly interface engineering—in achieving advanced functional properties in shape memory alloys.

Discussion

Achieving a simultaneous combination of a large elastocaloric effect and ultrahigh fatigue life has long been a central goal in the development of SMAs. In this study, we demonstrate that these typically conflicting properties can be reconciled through the introduction of epitaxially aligned Ti_4Ni_2O precipitates within a directionally solidified and textured B2 matrix. The resulting microstructure enables exceptional elastocaloric performance and mechanical durability, making the investigated alloy a promising candidate for next-generation solid-state refrigeration applications.

We propose a mechanism for the origin of the substantial elastocaloric effect observed in the alloy. First, the textured microstructure, fabricated via controlled directional solidification, enables a high average transformation strain of 6.1% under compressive loading —approaching the theoretical maximum of ~6.6% (see Fig. S3). This pronounced transformation strain is inherently linked to the crystallographic texture; prior studies have shown that SMA functionality is highly sensitive to grain orientation[41,55]. This is further evidenced by the significant anisotropy in superelastic behavior along and perpendicular to the SD, as presented in Fig. 2c. This anisotropic superelasticity and cyclic stability are consistent with both the stress–strain response and the microstructural evidence of preferential precipitate alignment (Fig. S9, S10). Compared with the perpendicular direction, compression along the SD benefits from the cooperative effect of $<001>_{B2}$ columnar texture and preferentially aligned Ti_4Ni_2O precipitates, which together lower the transformation stress, enhance transformation strain, and suppress defect accumulation. The enhanced superelastic strain along the SD indicates a higher degree of stress-induced martensitic transformability, thereby amplifying the elastocaloric response[34]. Second, the presence of epitaxially aligned Ti_4Ni_2O precipitates, sharing a fixed orientation relationship with the B2 matrix (Figs. 6 and S2), plays a critical role in suppressing dislocation activity. These precipitates impede slip-based plasticity and mitigate the accumulation of irreversible structural defects during cyclic loading[56]. As a result, the alloy is able to fully harness the potential of reversible SIMT to sustain large elastocaloric effects. Third, the columnar morphology of the Ti_4Ni_2O precipitates, aligned with the textured B2 grains along the SD (Fig. 1), supports an unobstructed SIMT within the textured microstructure. This alignment ensures minimal interference from secondary phases during transformation[57,58]. Together, these features allow the alloy to undergo nearly complete SIMT to B19′ martensite, yielding both high superelastic strain and a large adiabatic temperature change ΔT_{ad} during compression along the SD (Fig. 2c). In summary, the large elastocaloric effect originates from the alloy's exceptional transformability, facilitated by its tailored microstructure.

The high fatigue resistance of the alloy is proposed to derive from two key aspects: mechanical stability (structural fatigue resistance) and transformation reversibility (functional fatigue resistance). As shown in Fig. 1a, b, the microstructure features linearly aligned Ti_4Ni_2O precipitates embedded within columnar B2 grains, both oriented along the SD. This mutual texture effectively acts as a "reinforced concrete" architecture during compressive loading, delaying crack initiation and propagation, and significantly enhancing fatigue resistance across millions of loading cycles. Compression loading reduces crack-driving forces and enhances structural fatigue resistance[59]; in the present alloy, this benefit is complemented by the reinforced architecture, together delivering ultrahigh operational life. More critically, in-situ characterization reveals that the transformation in the present alloy proceeds via numerous heterogeneous B19′ martensite nucleation events at B2/Ti_4Ni_2O interfaces, regulated by interfacial strain fields, which collectively result in a spatially macroscopic homogeneous transformation behavior in sharp contrast to the abrupt, avalanche-like B2–B19′ transformation with multi-twinned growth reported in conventional TiNi alloys[50,60,61]. The spatial confinement imposed by Ti_4Ni_2O precipitates limits transformation to nanoscale domains, suppressing martensite clustering and eliminating the characteristic stress plateau[62,63]. Consequently, this regulated pathway yields a nonlinear stress–strain response with narrow hysteresis, indicative of a progressive and highly reversible SIMT that remains stable over high fatigue cycles. The exceptional cyclic stability arises not from a second-order continuous transition[64], but from a microstructurally regulated first-order pathway, where high-density Ti_4Ni_2O precipitates suppress strain localization and promote distributed nucleation, enabling a homogeneous, fatigue-resistant elastocaloric response. A slight initial ΔT_{ad} degradation (~2×10^6 cycles), caused by dislocation accumulation and residual nanoscale martensite from lattice incompatibility (see Fig. S7), is constrained by the aligned precipitates and regulated progressive transformation. The resulting defects with nano martensite and dislocation substructures concentrated near precipitate boundaries are able to locally modify transformation stresses, leading to a sequential (two-step) macroscopic response that further enhances reversibility and fatigue resistance during extended cycling.

In conclusion, a textured TiNi alloy containing high-density Ti_4Ni_2O precipitates was successfully synthesized through directional solidification. The resulting columnar B2 grains are aligned along the solidification direction, with epitaxial Ti_4Ni_2O precipitates uniformly distributed throughout the matrix. A well-defined orientation relationship of $\{100\}<011>_{B2}$ // $\{400\}<011>_{Ti_4Ni_2O}$ is maintained across the matrix-precipitate interface. Under compressive loading along the SD, the alloy exhibits remarkable superelasticity with a recoverable strain of 6.2% and a low modulus of 38.3 GPa. Furthermore, it retains a large ΔT_{ad} of ~15.9 K and a recoverable strain of 5.1% even after 10^7 loading-unloading cycles. These outstanding properties are enabled by the synergy between a highly transformable textured B2 parent phase and the reversibility induced by well-aligned textured precipitates. The findings underscore the potential of textured TiNi alloys with epitaxial Ti_4Ni_2O precipitates as efficient and durable elastocaloric materials, and offer a pathway for future design of high-performance SMAs through the integration of microstructural texturing and precipitation engineering.

Methods

Sample presentation

$Ti_{49}Ni_{51}$ (at. %) ingots were synthesized via vacuum arc melting of high-purity Ti and Ni, with trace oxygen intentionally introduced to promote the formation of Ti_4Ni_2O precipitates. The oxygen contents of the starting Ti and Ni materials were measured by inductively coupled plasma mass spectrometry (ICP-MS) to be 0.061 wt.% and 0.007 wt.%, respectively, resulting in a total oxygen concentration of 0.029 wt.% in the as-fabricated alloy. To ensure chemical homogeneity, each ingot was re-melted five times prior to casting into a water-cooled copper crucible. Directional solidification was achieved by installing a water-cooled system beneath the crucible base, establishing a vertical thermal gradient during solidification. For comparison, a commercial

polycrystalline $Ti_{49}Ni_{51}$ (at. %) alloy was also prepared. Specimens for both microstructural characterization and property evaluation were sectioned from the ingots using spark cutting.

Mechanical and elastocaloric testing

Compression tests were performed on cylindrical specimens with dimensions of 4 mm in diameter and 8 mm in height using an Instron 5969 universal testing machine. Tests were conducted at room temperature under a quasi-static loading-unloading strain rate of 10^{-3} s^{-1}, with strain tracked via a video extensometer. Fatigue performance was evaluated on an Instron 8801 fatigue test system under sinusoidal loading (10 Hz) for up to 10^7 cycles, with a maximum stress of 900 MPa, consistent with the superelastic measurements. For elastocaloric measurements, ΔT_{ad} during unloading was captured by a K-type thermocouple welded to the specimen surface. Samples were preloaded to 900 MPa at a strain rate of 10^{-3} s^{-1}, held briefly for thermal equilibrium, and then rapidly unloaded at a strain rate of 0.2 s^{-1} to ensure near-adiabatic conditions.

Structural and compositional analysis

All the samples for structural and compositional analysis were mechanically polished. SEM samples were etched using a mixture of 10% HF, 45% HNO_3, and 45% H_2O (by volume). TEM foils were prepared via twin-jet electropolishing in a solution of 20% H_2SO_4 and 80% CH_3OH (by volume) at 253 K. Phase identification was conducted using a Bruker D8 Advance X-ray diffractometer with Cu Kα radiation. Room-temperature microstructures were characterized using a FEI VERIOS 460 scanning electron microscope. Transmission electron microscopy investigations, including bright-field imaging, selected-area electron diffraction, energy-dispersive X-ray spectroscopy, and high-resolution TEM, were carried out on a JEOL JEM-F200 microscope. Crystallographic orientation and texture analyses were performed using a ZEISS Gemini 500 SEM equipped with an electron backscatter diffraction detector. EBSD data were processed using AztecCrystal software. Fast Fourier transformation, inverse fast Fourier transformation, and geometrical phase analysis were conducted using DigitalMicrograph software (version 3.43.3213.0).

In-situ transformation behavior analysis

Thermal transformation behavior was analyzed using a Netzsch 214 differential scanning calorimeter (DSC) across a temperature range of 153–263 K, at a constant heating and cooling rate of 10 K/min. To map strain evolution during compressive loading, digital image correlation was employed in conjunction with a high-speed camera. Tests were performed on rectangular specimens ($3 \times 3 \times 8$ mm^3), loaded to 900 MPa at a strain rate of 10^{-3} s^{-1} and unloaded to <10 MPa. In-situ loading XRD was conducted on a Rigaku MicroMax-007HF system equipped with a Mo rotating anode source ($\lambda = 0.7093$ Å). In-situ TEM cooling observations of martensitic transformation were carried out using a ThermoFisher Talos-F20 microscope, equipped with a Gatan 636 liquid nitrogen cooling holder. The TEM foil was held for 10 mins at each observation temperature to maintain thermal equilibrium.

Data availability

The authors declare that the experimental data generated in this study are provided within the paper and its Supplementary Information/Source Data files. Source data are provided with this paper.

References

1. Dupont, J.-L. The Role of Refrigeration in the Global Economy (2019), 38th Note on Refrigeration Technologies. *Tech. Rep.*https://doi.org/10.18462/iif.NItec38.06.2019 (2019).
2. McLinden, M. O. et al. Limited options for low-global-warming-potential refrigerants. *Nat. Commun.* **8**, 14476 (2017).
3. Moya, X. et al. Caloric materials for cooling and heating. *Science* **370**, 797–803 (2020).
4. Moya, X. et al. Too cool to work. *Nat. Phys.* **11**, 202–205 (2015).
5. Tušek, J. et al. The Elastocaloric Effect: A Way to Cool Efficiently. *Adv. Energy Mater.* **5**, 1500361 (2015).
6. Zhou, G. et al. A multi-material cascade elastocaloric cooling device for large temperature lift. *Nat. Energy* **9**, 862–870 (2024).
7. Goetzler, W. et al. Energy Savings Potential and RD&D Opportunities for Non-Vapor-Compression HVAC Technologies. *US Department of Energy, Office of Energy Efficiency and Renewable Energy, Building Technologies Office, USA*, https://doi.org/10.2172/1220817 (2014).
8. Zhou, G. et al. Achieving kilowatt-scale elastocaloric cooling by a multi-cell architecture. *Nature* **639**, 87–92 (2025).
9. Moya, X. et al. Caloric materials near ferroic phase transitions. *Nat. Mater.* **13**, 439–450 (2014).
10. Mañosa, L. & Planes, A. Materials with Giant Mechanocaloric Effects: Cooling by Strength. *Adv. Mater.* **29**, 1603607 (2016).
11. Bonnot, E. et al. Elastocaloric effect associated with the martensitic transition in shape-memory alloys. *Phys. Rev. Lett.* **100**, 125901 (2008).
12. Otsuka, K. & Ren, X. Physical metallurgy of Ti–Ni-based shape memory alloys. *Prog. Mater. Sci.* **50**, 511–678 (2005).
13. Mohd Jani, J. et al. A review of shape memory alloy research, applications and opportunities. *Mater. Des.* **56**, 1078–1113 (2014).
14. Cui, J. et al. Demonstration of high efficiency elastocaloric cooling with large ΔT using NiTi wires. *Appl. Phys. Lett.* **101**, 073904 (2012).
15. Eggeler, G. et al. Structural and functional fatigue of NiTi shape memory alloys. *Mater. Sci. Eng. A* **378**, 24–33 (2004).
16. Nargatti, K. & Ahankari, S. Advances in enhancing structural and functional fatigue resistance of superelastic NiTi shape memory alloy: A Review. *J. Intell. Mater. Syst. Struct.* **33**, 503–531 (2021).
17. Chluba, C. et al. Ultralow-fatigue shape memory alloy films. *Science* **348**, 1004–1007 (2015).
18. Dang, P. et al. Low-fatigue and large room-temperature elastocaloric effect in a bulk TiNiCu alloy. *Acta Mater.* **229**, 117802 (2022).
19. Lin, H. et al. Grain boundary and dislocation strengthening of nanocrystalline NiTi for stable elastocaloric cooling. *Scr. Mater.* **226**, 115227 (2023).
20. Hua, P. et al. Nanocomposite NiTi shape memory alloy with high strength and fatigue resistance. *Nat. Nanotechnol.* **16**, 409–413 (2021).
21. Hou, H. et al. Fatigue-resistant high-performance elastocaloric materials made by additive manufacturing. *Science* **366**, 1116–1121 (2019).
22. Li, X. et al. Fatigue-resistant elastocaloric effect in hypoeutectic TiNi58 alloy with heterogeneous microstructure. *Acta Mater.* **262**, 119464 (2024).
23. Chen, H. et al. Stable and large superelasticity and elastocaloric effect in nanocrystalline Ti-44Ni-5Cu-1Al (at%) alloy. *Acta Mater.* **158**, 330–339 (2018).
24. Xiao, F. et al. Improved functional fatigue resistance of single crystalline NiTi micropillars with uniformly oriented Ti3Ni4 precipitates. *Int. J. Plast.* **160**, 103480 (2023).
25. Wang, X. et al. Improved functional stability of a coarse-grained Ti-50.8 at.% Ni shape memory alloy achieved by precipitation on dislocation networks. *Scr. Mater.* **163**, 57–61 (2019).
26. Lu, H. et al. Simultaneous enhancement of mechanical and shape memory properties by heat-treatment homogenization of Ti_2Ni precipitates in TiNi shape memory alloy fabricated by selective laser melting. *J. Mater. Sci. Technol.* **101**, 205–216 (2022).
27. Lu, B. et al. Influence of microstructure on phase transformation behavior and mechanical properties of plasma arc deposited shape memory alloy. *Mater. Sci. Eng., A* **736**, 130–136 (2018).

28. Miyazaki, S. et al. The habit plane and transformation strains associated with the martensitic transformation in Ti-Ni single crystals. *Scr. Metall.* **18**, 883–888 (1984).
29. Inoue, H. et al. Texture and shape memory strain in TiNi alloy sheets. *Acta Mater.* **44**, 4825–4834 (1996).
30. Hou, R. et al. The role of texture on superelasticity and elastocaloric effect in severely rolled Ti-44Ni-5Cu-1Al (at%) shape memory alloy. *Scr. Mater.* **209**, 114334 (2022).
31. Pang, G. et al. Anisotropy of elastocaloric cooling effect in equal atomic ratio NiTi alloy with crystallographic texture. *J. Mater. Res. Technol.* **30**, 1128–1135 (2024).
32. Xiao, F. et al. Orientation dependence of elastocaloric effect in an aged Ni-rich Ti-Ni alloy. *Scr. Mater.* **168**, 86–90 (2019).
33. Zhang, G. et al. Giant elastocaloric effect in a Mn-rich Ni44Mn46Sn10 directionally solidified alloy. *Appl. Phys. Lett.* **116**, 023902 (2020).
34. Zhang, G. et al. Colossal elastocaloric effect in a <001>A oriented Ni49Mn33Ti18 polycrystalline alloy. *Scr. Mater.* **234**, 115584 (2023).
35. Zhang, G. et al. Giant elastocaloric effect covering a wide temperature region in a directionally solidified Ni50Mn30Ti20 alloy. *Scr. Mater.* **237**, 115725 (2023).
36. Yang, J. et al. Crystallography of stress-induced martensitic transformation and giant elastocaloric effect in a <001>A textured Ni27Cu21Mn46Sn6 shape memory alloy. *Acta Mater.* **263**, 119546 (2024).
37. Wang, H. et al. Large elastocaloric effect covering a broad temperature window in a composition-graded Ni50Mn31.5Ti18.5 alloy prepared by magnetic field-assisted directional solidification. *Acta Mater.* **274**, 120020 (2024).
38. Zhu, X. et al. Superelasticity and elastocaloric effect in a textured Ti-Nb-Zr-Ta alloy with narrow stress hysteresis. *J. Alloy. Compd.* **956**, 170291 (2023).
39. Zhu, X. et al. Meso-scopically homogeneous superelastic transformation and related elastocaloric effect in a textured Ti-based shape memory alloy. *Intermetallics* **164**, 108109 (2024).
40. Xiao, F. et al. Giant elastic response and ultra-stable elastocaloric effect in tweed textured Fe-Pd single crystals. *Acta Mater.* **223**, 117486 (2021).
41. Gall, K. & Sehitoglu, H. The role of texture in tension–compression asymmetry in polycrystalline NiTi. *Int. J. Plast.* **15**, 69–92 (1999).
42. Gall, K. et al. Tension–compression asymmetry of the stress–strain response in aged single crystal and polycrystalline NiTi. *Acta Mater.* **47**, 1203–1217 (1999).
43. Ti4Ni2O Crystal Structure: Datasheet from "PAULING FILE Multinaries Edition – 2022" in SpringerMaterials (https://materials.springer.com/isp/crystallographic/docs/sd_1211718). (eds Villars P., Cenzual K.). Springer-Verlag Berlin Heidelberg & Material Phases Data System (MPDS), Switzerland & National Institute for Materials Science (NIMS), Japan.
44. Ti2Ni Crystal Structure: Datasheet from "PAULING FILE Multinaries Edition – 2022" in SpringerMaterials (https://materials.springer.com/isp/crystallographic/docs/sd_0252202). (eds Villars P., Cenzual K.). Springer-Verlag Berlin Heidelberg & Material Phases Data System (MPDS), Switzerland & National Institute for Materials Science (NIMS), Japan.
45. Zhu, X. et al. Enhanced elastocaloric stability in NiTi alloys under shear stress. *Mater. Sci. Eng., A* **838**, 142787 (2022).
46. Kim, Y. et al. Elastocaloric effect in polycrystalline Ni 50 Ti 45.3 V 4.7 shape memory alloy. *Scr. Mater.* **144**, 48–51 (2018).
47. Tušek, J. et al. Elastocaloric effect vs fatigue life: Exploring the durability limits of Ni-Ti plates under pre-strain conditions for elastocaloric cooling. *Acta Mater.* **150**, 295–307 (2018).
48. Zhang, X. et al. Enhanced cyclability of superelasticity and elastocaloric effect in Cu and B co-doped Co-Ni-Ga shape memory alloys. *J. Alloy. Compd.* **918**, 165633 (2022).
49. Zheng, L. et al. Effects of Lüders-like bands on NiTi fatigue behaviors. *Int. J. Solids Struct.* **83**, 28–44 (2016).
50. Li, Y. et al. A mechanical criterion for Lüders-type deformation of polycrystalline NiTi. *Acta Mater.* **245**, 118604 (2023).
51. Liang, Q. et al. Strain states and unique properties in cold-rolled TiNi shape memory alloys. *Acta Mater.* **231**, 117890 (2022).
52. Liang, Q. et al. Low-fatigue large elastocaloric effect in NiTi shape memory alloy enabled by two-step transition. *Scr. Mater.* **252**, 116239 (2024).
53. Hÿtch, M. J. et al. Quantitative measurement of displacement and strain fields from HREM micrographs. *Ultramicroscopy* **74**, 131–146 (1998).
54. Wang, D. et al. Phase field simulation of martensitic transformation in pre-strained nanocomposite shape memory alloys. *Acta Mater.* **164**, 99–109 (2019).
55. Gall, K. et al. On the mechanical behavior of single crystal NiTi shape memory alloys and related polycrystalline phenomenon. *Mater. Sci. Eng., A* **317**, 85–92 (2001).
56. Zhang, J. et al. Leaf-like dislocation substructures and the decrease of martensitic start temperatures: A new explanation for functional fatigue during thermally induced martensitic transformations in coarse-grained Ni-rich Ti–Ni shape memory alloys. *Acta Mater.* **60**, 1999–2006 (2012).
57. Allafi, J. K. et al. The mechanism of multistage martensitic transformations in aged Ni-rich NiTi shape memory alloys. *Acta Mater.* **50**, 793–803 (2002).
58. Khalil-Allafi, J., Dlouhy, A. & Eggeler, G. Ni_4Ti_3-precipitation during aging of NiTi shape memory alloys and its influence on martensitic phase transformations. *Acta Mater.* **50**, 4255–4274 (2002).
59. Hou, H. et al. Overcoming fatigue through compression for advanced elastocaloric cooling. *MRS Bull.* **43**, 285–290 (2018).
60. Song, Y. et al. A lightweight shape-memory alloy with superior temperature-fluctuation resistance. *Nature* **638**, 965–971 (2025).
61. Song, Y. et al. Enhanced reversibility and unusual microstructure of a phase-transforming material. *Nature* **502**, 85–88 (2013).
62. Zhang, Z. et al. Nonhysteretic superelasticity of shape memory alloys at the nanoscale. *Phys. Rev. Lett.* **111**, 145701 (2013).
63. Liu, L. et al. Direct observation of hierarchical nucleation of martensite and size-dependent superelasticity in shape memory alloys. *Nanoscale* **6**, 2067–2072 (2014).
64. Chen, H. et al. Unprecedented non-hysteretic superelasticity of [001]-oriented NiCoFeGa single crystals. *Nat. Mater.* **19**, 712–718 (2020).

Acknowledgements

This work was supported by the Science Challenge Project of China (No. TZ2025009 - X.D. and Q.L.), and the National Natural Science Foundation of China (No. W2411048 - X.D., No. 52201228 - Q.L., No. 52425104 and No. 52394163 - S.L.). D.W. would like to acknowledge the support from the Outstanding Youth Fund of Shaanxi Province (No. 2024JC-JCQN-45), the Qin Chuangyuan "Scientist + Engineer" Team Building Project (No. 2023KXJ-183), and 111 Project (No. BP0618008).

Author contributions

Q.L. was the lead scientist of the study and proposed the core concept. X.L. performed sample preparation and property testing experiments as well as SEM observation, XRD, and DIC measurement. Q.L. performed the HR-TEM and in-situ TEM characterizations. C.L. performed the visualization of the transformation strain distribution. X.L. and Q.L. wrote the paper, with contributions from C.L., D.W., S.L., and X.D. X.D. supervised the research. All authors contributed to the discussion.

Competing interests

The authors declare no competing interests.

Additional information

Supplementary information The online version contains supplementary material available at https://doi.org/10.1038/s41467-026-68835-0.

Correspondence and requests for materials should be addressed to Qianglong Liang or Xiangdong Ding.

Peer review information *Nature Communications* thanks Mingfang Qian and the other anonymous reviewer(s) for their contribution to the peer review of this work. A peer review file is available.